Journal of Magnetism and Magnetic Materials 524 (2021) 167662

Contents lists available at ScienceDirect

Journal of Magnetism and Magnetic Materials

journal homepage: www.elsevier.com/locate/jmmm

Research articles

Co-Cd nanoferrite for high frequency application with phenomenal rise in DC resistivity

Pydiraju T.R.K.[a,b,*], Srinivasa Rao K.[c], Appa Rao P.[a,b], Chaitanya Varma M.[d,*], Satish Kumar A.[e], H. Rao K.[b]

[a] Physics Department, Dadi Institute of Engineering & Technology, Anakapalli 531002, A.P, India
[b] Physics Department, Andhra University, Visakhapatnam 530003, A.P, India
[c] Physics Department, PBN College, Nidubrolu 522124, A.P, India
[d] Department of Electronics and Physics, Institute of Science, GITAM (Deemed to be University), Visakhapatnam 530045, A.P, India
[e] Physics Department, IIIT, RGUKT, Nuzividu 521 202, A.P, India

ARTICLE INFO

Keywords:
Nanoferrites
Sol-gel process
Cation distribution
Saturation magnetization
DC resistivity

ABSTRACT

The communication concentrates on the possibility of developing a composition suitable for high-frequency operation as a magnetic core through an extensive understanding of the cation distribution of cobalt ferrite containing cadmium. The samples having a composition, $Co_{1-x}Cd_xFe_2O_4$, were processed by the sol–gel method using polyvinyl alcohol (PVA) as a chelating agent and characterized by standard techniques. Substantial growth in specific saturation magnetization from 82.2 emu/g to 99 emu/g and DC resistivity from 1.54×10^6 Ω-cm to 1.34×10^{11} Ω-cm, requisite characteristics for high-frequency application were provided with increasing concentration of cadmium. The average crystallite size ranging from 5.7 nm to 17 nm has been estimated by X-ray diffraction patterns using Williamson-Hall analysis. The proposed cation distribution based on saturation magnetization data established the amount of cadmium occupying the tetrahedral sites of spinel lattice, which was well supported by the variation of DC resistivity with cadmium. The unparalleled matching between the experimentally observed lattice constant and that provided by the proposed cation distribution as well as Rietveld refinement confirms the amounts of cadmium entering tetrahedral and octahedral sites of the spinel lattice. All the samples of cadmium substituted cobalt ferrite assure their suitability for high frequency application with the pertinent properties.

1. Introduction

With the advent of nanotechnology and advances in synthesis, ferrites have taken a revolutionary path in the form of magnetic nanoparticles with their spectacular properties and a new era has begun in electronic industry and biotechnology with the innovative applications [1–6]. Exploring novel techniques of preparation and adopting them scrupulously to enhance the physical properties suitable for present-day applications is an unending process for a dedicated researcher.

Cobalt ferrite, in bulk form finds a wide range of applications in magnetostrictive sensors, transducers, and magnetic recording devices because of its moderate saturation magnetization, high coercivity, and large magneto-crystalline anisotropy [7,8]. The stupendous modification in certain properties like saturation magnetization, initial permeability, particle size and DC resistivity by transferring the bulk material into nanostructure makes the cobalt ferrite a potential candidate for magnetic data storage [9], targeting drug delivery carriers [10], biosensors [11] and heating agents of magnetic hyperthermia [12] and high-frequency applications [13]. The anticipated changes in several parameters for any particular application can be made available to a larger extent if the material is synthesized in nano form through careful attention by controlling the method of processing. For instance, bulk nickel-zinc ferrite found unsuitable as a magnetic core beyond 100 MHz was accomplished in nano form to have the operating frequencies close to 20 GHz [14].

There exist several methods for the preparation of ferrite nanoparticles, namely, ball milling [15], co-precipitation [16], reverse micelles [17], hydrothermal [18], polymeric precursor [19], sol–gel and so on [20,21]. Although most of the methods are capable of providing nanoparticles of desired size and microstructure, the cheapest and cost-

* Corresponding authors at: Physics Department, Dadi Institute of Engg. & Technology, Anakapalli 531002, A.P, India (T.R.K. Pydiraju).
E-mail addresses: trkpydiraju@gmail.com (T.R.K. Pydiraju), cmudunur@gitam.edu (M. Chaitanya Varma).

https://doi.org/10.1016/j.jmmm.2020.167662
Received 28 August 2020; Received in revised form 22 November 2020; Accepted 7 December 2020
Available online 16 December 2020

effective are wet chemical methods [1]. The sol–gel method was proved to be the superior one among the available wet chemical methods in yielding the least sized nanoparticles at low temperatures with uniform distribution and controlled shape [22].

The size dependent properties of nanoparticles, highly sensitive to the presence of impurity ions find several exciting opportunities in the fields close to biomedicine [23]. The modifications that occur in these nanoparticles are exceptional, unlike those of the bulk materials. Recently, single-domain nanoparticles of Co-Zn ferrite were proved to be suitable for self-controlled magnetic hyperthermia with high specific saturation magnetization and Curie temperature close to therapeutic temperature [24]. On the other hand, Eu/Nd-substituted Mn-Zn ferrite nanoparticles of size 7 to 8 nm were found more effective as anticancer agents because of their large specific surface area (173,500 m^2/g) [25]. In another study, boron rich compound attached to the modified surface of the Fe_3O_4 nanoparticles were proved suitable for cancer treatment by boron-neutron capture therapy [26,27]. In nano $Ni_{1-x}Zn_xFe_2O_4$ (x = 0.25, 0.5 and 0.75) the particles possessing higher saturation magnetization showed higher heating efficiency in alternating magnetic field, an essential requirement in clinical hyperthermia to minimize the dosages of the material [28].

The superior properties associated with the least sized particles and their usage in various applications not only confined to spinel systems, but extended to other areas dealing with hexaferrites, garnets and nanocomposites [29–31]. The systems exhibit remarkable electrical and magnetodielectric properties suitable for high frequency applications up to several megahertz. The large scope invariably combined with the composition selection, preparation and controlling the properties to a satisfactory level draws towards the present investigation of spinel ferrites.

Several attempts have been made by a number of researchers to understand the particle size related magnetic and electrical properties [32–36]. Specific saturation magnetization and DC resistivity of a number of ferrites were determined using a variety of methods along with particle size. For instance, in high frequency applications, high saturation magnetization and high DC resistivity are desirable parameters for smaller particle sizes. It has become a difficult task to attain all the required characteristics suitable for a specific application in a single composition. If one succeeds in achieving high resistivity, the other parameters will be deteriorated [37,38]. Moreover, reaching saturation magnetization above 80 emu/g and resistivity above 10^8 Ω-cm for a particle size less than 20 nm is a Herculean task for many excepting one or two researchers [13,39]. The present work is a systematic attempt to bestow the samples with high specific saturation magnetization of about 99 emu/g, and DC resistivity10^9 Ω-cm for a particle size less than 10 nm.

In cobalt ferrite, the substitution of zinc in place of cobalt shows that zinc prefers to occupy tetrahedral sites throughout its concentration and completely fills the tetrahedral sites irrespective of the ions present at A-site [24]. Whereas, the diamagnetic magnesium, with its stronger preference to octahedral sites [32], occupies the B-sites throughout its concentration irrespective of the ions present at B-sites. Although zinc and magnesium are divalent and diamagnetic, their inclusion in cobalt ferrite shows no trace of parallel trends among the properties due to their preferences to occupy different sites. For instance, partial replacement of cobalt by zinc enhances saturation magnetization while magnesium reduces the magnetization invariably [24,32]. Instead, if impurity ions enter both the tetrahedral and octahedral sites, the properties may increase or decrease depending upon their distribution which needs a meticulous investigation.

There have been varied opinions about the amount of cobalt present at tetrahedral sites in cobalt ferrite where the reported amount of cobalt lies in between zero to 55% [40–46]. The substitution of zinc or magnesium cannot determine the amount of cobalt present at the tetrahedral site in pure cobalt ferrite because zinc occupies A-sites, whereas magnesium occupies B-sites. The exact amount of cobalt present at the tetrahedral site of the cobalt ferrite may be obtained provided the diamagnetic ion used for substitution should be small in amount and capable of replacing cobalt at both the A and B-sites. With a view of procuring information in this direction, cadmium impurity has been selected for the present study and varied in smaller amounts in place of cobalt in cobalt ferrite.

In respect of cadmium, other divalent and diamagnetic impurities, the available information related to the site occupancy of cadmium in cadmium substituted cobalt ferrite nanoparticles is insufficient, and the results are often conflicting [47]. In $Co_{1-x}Cd_xFe_2O_4$ ($0 \leq x \leq 1$) bulk ferrite system, several researchers reported that entire Cd^{2+} ions prefer to occupy only the tetrahedral sites [42,44]. A study in nano $Co_{1-x}Cd_xCr_{0.5}Fe_{1.5}O_4$ shows Cd^{2+} ions occupy both A and B-sites [48]. Nano $Co_{1-x}Cd_xFe_2O_4$ ($0 \leq x \leq 1$) was observed to change from partially inverse to a normal spinel structure with the cadmium substitution [47].

The saturation magnetization trends reported by different researchers are also quite contradictory [44,48,49]. For instance, the specific saturation magnetization and the Curie temperature were noticed to increase monotonically with increasing diamagnetic cadmium throughout its concentration up to x = 0.9 in $Co_{1-x}Cd_xFe_2O_4$ and the increase was attributed to strong A-B super-exchange interaction, which is rather unbelievable [50]. Contrary to this, the Mossbauer study of $Co_{1-x}Cd_xFe_2O_4$ showed paramagnetic doublets for higher concentrations of cadmium indicating a clear weak exchange interaction between A-B site ions [42]. A few reports suggest that the dilution of tetrahedral sites with diamagnetic ions weakens A-B interaction [24,47]. Hence, it was opined that cadmium impurity might bring a new interesting picture, unlike zinc and magnesium impurity in cobalt ferrite.

The shifting of operating frequency to higher side may become practical with small-sized particles with increased resistivity and saturation magnetization. However, obtaining a material with all its requisite properties is a challenging task and needs more information about its microstructure and site occupancy of cations for which cation distribution helps superbly. For promoting a relevant material with the desired characteristics useful for high-frequency application, it is imminent to have a complete understanding of the distribution of cations among the available interstitial sites of the spinel structure.

A systematic investigation is planned to develop a nanomaterial with superior improvement in specific saturation magnetization and DC resistivity through a comprehensive understanding of the cation distribution of the smallest sized cobalt cadmium ferrite processed by sol–gel method.

2. Synthesis and characterization

Co_{1-x} $Cd_xFe_2O_4$ nanoparticles with x varying from 0.000 to 0.280 in steps of 0.035 were synthesized by sol–gel method from the analytical reagent grade nitrates of iron, cobalt and cadmium. Polyvinyl alcohol was used as a chelating agent keeping the weight ratio of ferrite to PVA as 1:3. As described in our earlier publications [22,24], the as-prepared powders were annealed at 400 °C for an hour to initiate the formation of the ferrite. The annealed powders were thoroughly ground and made into pellets and toroids using a small amount of polyvinyl alcohol as a binder before heat-treated for another hour at 1050 °C in a programmable muffle furnace.

Panalytical X'Pert Pro, powder X-ray diffractometer with Cu-Kα radiation was used to identify single-phase spinel structure of all the prepared compositions. The mean particle size of the samples was estimated using a JOEL JEM 200CX model transmission electron microscope (TEM) operated at 120 kV. Room temperature magnetic hysteresis loops were obtained with the help of a Quantum Design (USA) PPMS vibrating sample magnetometer operated at the maximum magnetic field of ±30kOe. The atomic percentages of elements present in each composition were determined with the field emission scanning electron microscope (FESEM) equipped with energy dispersive X-ray spectroscopy (EDX). Curie temperature was estimated from the temperature dependence of the initial permeability, recorded at a constant frequency

of 100 kHz using a high-frequency LCR meter. Agilent E4991A RF impedance analyzer was employed for measuring the variation of initial permeability as a function of frequency on toroidal samples at room temperature. The two-probe method was used to estimate the DC resistivity with the accurate measurement of current by the dielectric impedance analyzer (BDS50 model). The experimental density was obtained from using Archimedes' principle for each sample and the X-ray density was calculated using the equation $d_{X\text{-}ray} = 8M/Na^3$, where M is the molecular weight, N is the Avogadro's number, and 'a' is the lattice constant.

3. Results and discussion

3.1. XRD

Fig. 1a shows the powder XRD patterns of $Co_{1-x}Cd_xFe_2O_4$ nanoparticles and the observed fundamental reflections from the planes (111), (220), (331), (222), (400), (422), (511), (440), and (533) characterize the cubic spinel structure of the prepared samples. The reflections related to the basic cadmium-free cobalt ferrite, are closely matched with those of the cobalt ferrite (JCPDS card no. 22-1086) and affirm single-phase spinel structure with no traces of impurity phases. The diffraction peaks have been observed to shift slightly towards the smaller angle with increasing cadmium content, as shown in Fig. 1b. The shift increases the interplanar spacing and thereby increases the lattice constant.

The lattice constant (a_{exp}) has been determined from the diffraction angles of each pattern by minimizing the error in its calculation, taking the Nelson-Riley function into consideration. The observed linear increase in lattice constant from 8.3895 Å to 8.4713 Å with the increase of cadmium content confirms its occupancy into the spinel lattice, and the same has been ascribed to the larger radius of Cd^{2+} ion (0.78 Å/0.95 Å at A-sites/B-sites), replacing the Co^{2+} ion (0.58 Å/0.745 Å at A-sites/B-sites) of the smaller ionic radius. A similar kind of argument was presented by other researchers [47,48].

The estimated gradual increase in X-ray density ($d_{X\text{-}ray}$) (Table 1) with increasing cadmium content was due to massive cadmium ions occupying the place of less massive cobalt ions. However, the observed decrease in experimental density (d_{Bulk}), was attributed to formation of pores due to volatilization of cadmium possessing lower melting point (321.1 °C) as compared to that of cobalt (1495 °C). The loss of cadmium has been verified by EDX, discussed in Section 3.5.3.

The crystallite size and micro strain are the main contributions for the broadening of the diffraction peak. The size and strain components can be separated from the peak broadening, full width at half maximum (FWHM) of the XRD lines using the following equation [51],

$$\beta = \frac{K\lambda}{D\cos\theta} + 4\varepsilon\tan\theta \quad (1)$$

In the equation, λ represents the X-ray wavelength, θ gives the position of the diffraction peak, ε is the strain, D is the crystallite size, and K is the shape factor or Scherrer constant.

Rewriting the above equation

$$\frac{\beta\cos\theta}{\lambda} = \frac{K}{D} + \frac{4\varepsilon\sin\theta}{\lambda} \quad (2)$$

The diffraction peaks are considered as Lorentzian to obtain FWHM corresponding to each peak. Crystallite size has been estimated using Williamson-Hall plots considering the shape factor equal to 1. Considering the shape factor K = 1, a close agreement was observed between the particle size and crystallite size in our earlier work [52] and the same view has been applied to the present case. The argument is justified by the works of other researchers [51,53,54]. With increasing cadmium concentration, the observed gradual decrease in crystallite size from 16.6 nm to 5.7 nm together with increasing compressive strain was shown in Table 1 which gives other parameters lattice constant, theoretical and experimental densities and porosity of $Co_{1-x}Cd_xFe_2O_4$. The matching between the calculated crystallite size and the particle size from TEM measurements, given in the next section 3.2 also supports the above understanding.

Table 1
Lattice constant, Crystallite size and strain from Williamson Hall (W-H) plots, X-ray density ($d_{X\text{-}ray}$), bulk density (d_{Bulk}) and percentage of porosity.

x	Lattice constant (a_{exp}) Å	W-H plots		$d_{X\text{-}ray}$ (g/cm^3)	d_{Bulk} (g/cm^3)	Porosity (%)
		Crystallite size (nm)	Strain (10^{-4})			
0.000	8.3895	16.6	−3.69	5.2783	4.7993	9.1
0.035	8.3966	14.6	−5.51	5.3070	4.7913	9.7
0.070	8.4023	11.8	−6.55	5.3381	4.7896	10.3
0.105	8.4187	9.2	−12.8	5.3486	4.7006	12.1
0.140	8.4194	7.5	−19.4	5.3889	4.6209	14.3
0.210	8.4538	6.5	−22.6	5.4057	4.4238	18.2
0.280	8.4713	5.7	−25.2	5.4540	4.3105	21.0

3.2. Estimation of particle size

The transmission electron micrographs and particle size distribution histograms of $Co_{1-x}Cd_xFe_2O_4$ (x = 0.00, 0.07, 0.14 and 0.28) powders

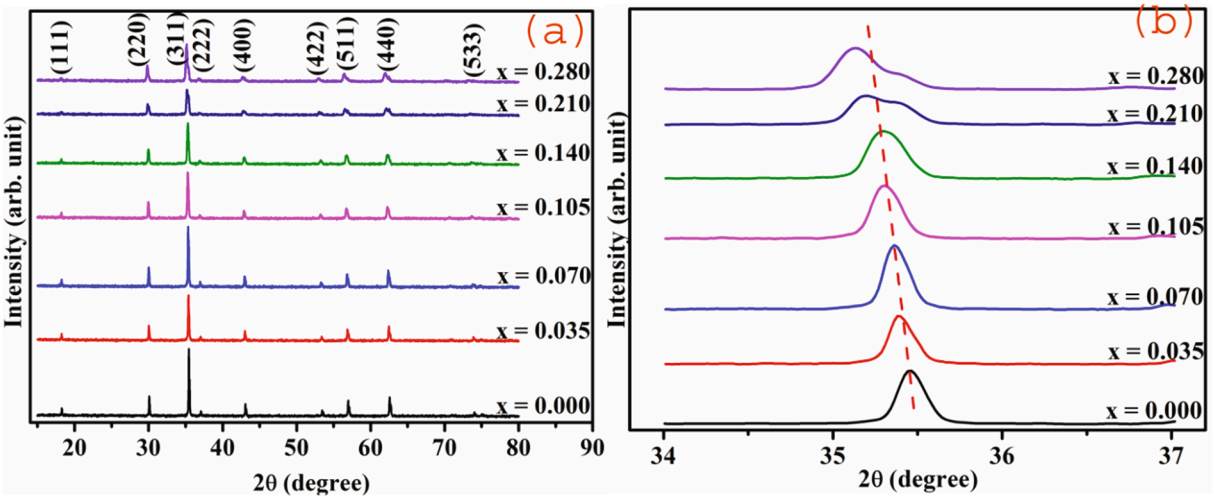

Fig. 1. (a) X-ray diffractograms and (b) magnified (311) peak of $Co_{1-x}Cd_xFe_2O_4$.

have been presented in Fig. 2. In estimating the particle size, ImageJ software has been used considering the linear dimensions of several particles of two image pictures at different regions of each sample. The distribution of particle size is fitted with a log-normal function to evaluate the mean size of the particle. The images reflect the agglomerated nature of the primary particles to a certain extent. The estimated average particle size in the range of 17 nm to 5.7 nm agrees well with the crystallite size obtained from the XRD patterns (Table 1).

It is clear from the particle size distributions (Fig. 2), shown in transmission electron micrographs number of smaller particles is observed with increasing cadmium concentration on the lower side of the particle size with which more number of grains and grain boundaries are expected in the samples having higher cadmium concentration. The influence of cadmium in reducing the particle size has been in parallel with other systems discussed by many researchers [55,56]. The increased porosity (Table 1) might be the underlying cause for the observed decrease in particle size where the driving force is annulled by the pores and promoting the grain boundary thickness [32].

3.3. Specific saturation magnetization

Fig. 3 shows the field dependence of specific magnetization curves for $Co_{1-x}Cd_xFe_2O_4$ ferrite nanoparticles at room temperature. The specific magnetization increases sharply at very low applied magnetic field around 1 kOe and thereafter increased slowly up to saturation. Further, all samples have been observed to attain saturation in the applied magnetic field of 30 kOe.

The variation in specific saturation magnetization as a function of cadmium concentration is shown in Fig. 4. The specific saturation magnetization has been observed to increase from 82.2 emu/g to 99 emu/g with increasing cadmium concentration up to $x = 0.105$ followed by a decrease beyond $x = 0.105$. A similar observation was reported by S. Bhukal et al. [57] in $Co_{0.5}Zn_{0.5}Cd_xFe_{2-x}O_4$ nanoferrites. Further, the observed specific saturation magnetization values are very close to those reported by S. Noor et al. [44] at 5 K in a magnetic field of 50 kOe for the Co-Cd ferrite system, indicating the capability of the PVA assisted sol–gel method in yielding higher saturation magnetization for ferrite material.

The observed specific saturation magnetization versus cadmium concentration can be explained on the basis of the exchange interactions prevailed among the ions of the tetrahedral (A) and octahedral (B) sites in the lattice for which the distribution of cations of these sites is necessary. In general, there exist three types of exchange interactions among the magnetic ions present at A and B sites, namely A-B, B-B and A-A interactions, out of which A-B interaction is the strongest, B-B is stronger and A-A is the weakest. In case A-B interaction persists in the sample, the difference in the magnetic moments of A and B sub lattices gives the net magnetic moment of the unit cell according to Neel's model.

To explain the observed variation of specific saturation magnetization, possible mechanisms have been considered with reference to the site occupancy of cadmium ions into the lattice.

Based on the accurate measurements made by several researchers [32,58], the general formula for cobalt ferrite nanoparticles can be written as $(Co_\delta Fe_{1-\delta})\ [Co_{1-\delta}Fe_{1+\delta}]\ O_4$ with nearly 20% of cobalt at A sites. In the present investigation, it is to be noted that the maximum amount of cadmium substituted in place of cobalt is 28%.

If cadmium ions replace cobalt until it is available at A-site, the A-site magnetic moment decreases and no change occurs in B-site magnetic moment. After complete depletion of Co^{2+} ions at A-sites, Cd^{2+} ions continue to enter into A-sites and transfer an equal amount of Fe^{3+} ions to B-sites. This process increases the B-site magnetic moment and saturation magnetization gradually increases. As such, an increase in saturation magnetization has not been observed in the present system, the possibility of cadmium ions entering into A-site has been ruled out.

If cadmium ions enter the B sub-lattice only, the substitution of octahedral Co^{2+} ions by Cd^{2+} ions dilutes the B sub-lattice magnetic moment. The dilution of B sub-lattice magnetic moment weakens the A-B super-exchange interaction and consequently results in a reduction in the saturation magnetization. A gradual fall in saturation magnetization is expected throughout the cadmium concentration due to the reduction of the magnetic moment of the B sub-lattice with more diamagnetic content. This possibility has also been ruled out based upon the observed variation.

In another possible mechanism, cadmium ions may occupy both the tetrahedral and octahedral sites in equal amounts without affecting A-B exchange interaction. The process reduces the magnetic moments of both the sub-lattices resulting in a constant magnetic moment of the system. This possibility has also been ruled out based upon the observed variation.

If cadmium enters the A-sites and replaces Co^{2+} ions present at that site, the A-site magnetic moment decreases without affecting the magnetic moment of the B-site. The process shows an increase in the net magnetization with increasing cadmium concentration.

The replacement of cobalt continues until it is depleted at A-sites, and thereafter, Cd^{2+} ions replace cobalt ions at the B-sites with which a gradual decrease in specific saturation magnetization is expected with increasing cadmium content. This kind of mechanism supports the observed variation of specific saturation magnetization (Fig. 4) with cadmium concentration. In the present investigation, the maximum amount of cadmium added in place of cobalt is 28%, which is not too high to affect the A-B interaction. The observed variation in specific saturation magnetization with its maximum value reiterates the amount of cobalt present at A-sites corresponds to $x = 0.105$, which is equal to 10.5% of cobalt in cobalt ferrite. For higher concentration above $x = 0.105$, Cd^{2+} starts entering B sites and causes the magnetic moment of the B-site to decrease without affecting the magnetic moment of the A-site. Thus, the decrease in net magnetic moments of both (A and B) the sites causes a decrease in the saturation magnetization with the cadmium content.

The magneto-crystalline anisotropy constant (K), and the Curie temperature support the cadmium dependence of specific saturation magnetization.

The determination of magneto-crystalline anisotropy constant can be worked out using experimental values of coercivity (Hc) (Table 2) and magnetization at 30 kOe (M_S) from the relation [59],

$$K = \frac{H_C \times M_S}{0.96}. \quad (3)$$

The estimated 'K' value has been noticed to increase from1.47×10^6 erg/cm^3 to 2.53×10^6 erg/cm^3 with increasing cadmium content up to $x = 0.105$, followed by a decrease beyond $x = 0.105$ (Fig. 5).

In general, the material having cobalt ions at B-site exhibits a very large magnetic anisotropy [32]. The observed gradual decrease in magnetic anisotropy beyond cadmium concentration $x = 0.105$ indicates the entry of Cd^{2+} ions into octahedral sites which happens due to the depletion of Co^{2+} ions at A- site. Hence, the decreasing trend in magnetic anisotropy with increasing cadmium content is due to the gradual fall of cobalt content at octahedral sites.

3.4. Curie temperature

Fig. 6 shows the variation of initial permeability as a function of temperature at constant frequency, 100 kHz, from which the Curie temperature has been determined for all the samples. The temperature corresponding to a sudden drop in the initial permeability appeared is known as Curie temperature.

The linear decrease of Curie temperature from 470 °C to 389 °C (Fig. 7) has been attributed to cadmium site occupancy and consequent exchange interactions. As A-site cobalt is replaced by cadmium up to its concentration $x = 0.105$, the dilution of the magnetic ions at that site causes the decrease in Curie temperature by weakening the exchange

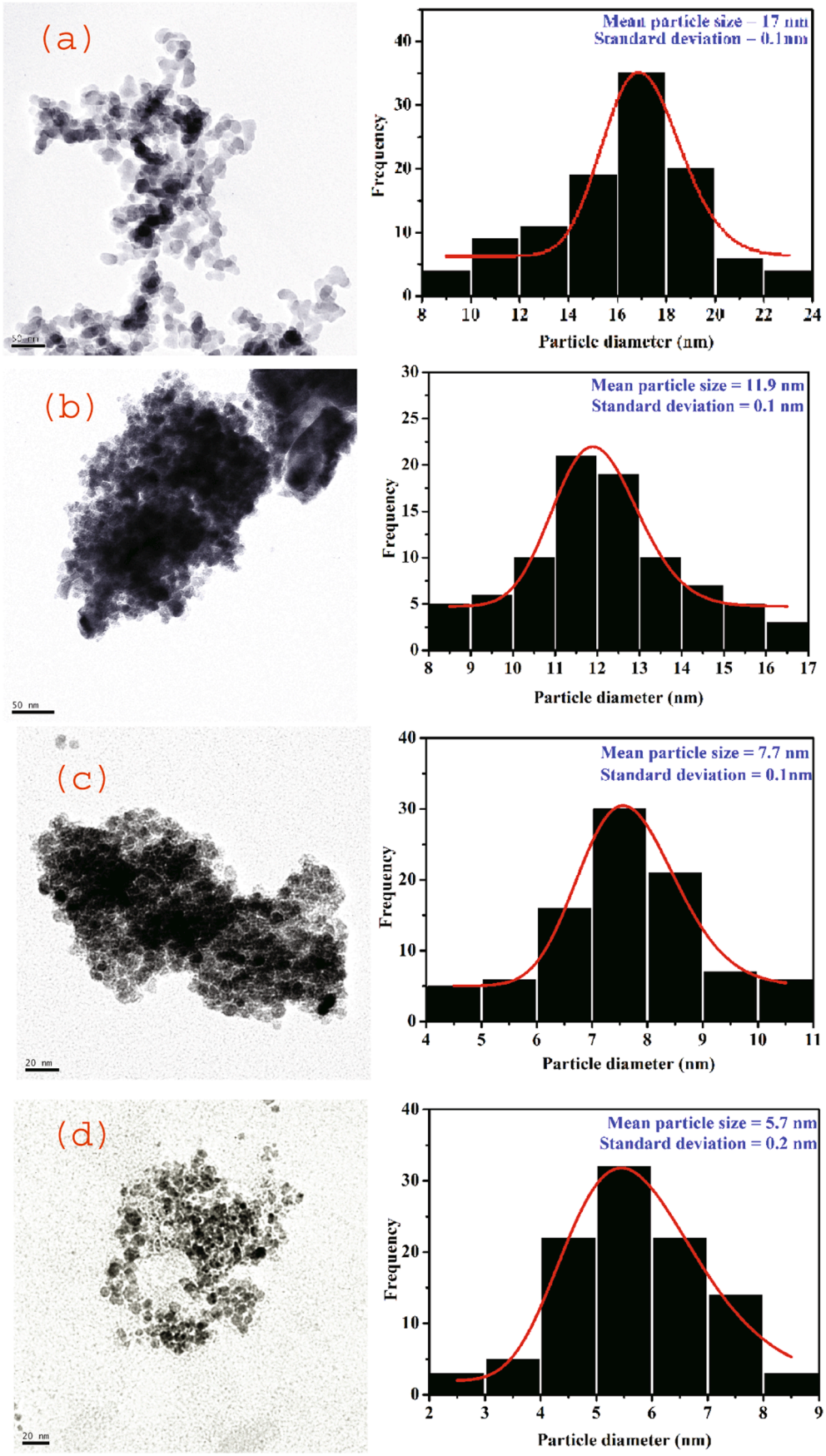

Fig. 2. The TEM images and particle size distribution of $Co_{1-x}Cd_xFe_2O_4$ powders: x = 0.00 (a), x = 0.07 (b), x = 0.14 (c) and x = 0.28 (d). The solid line is a log-normal function fit.

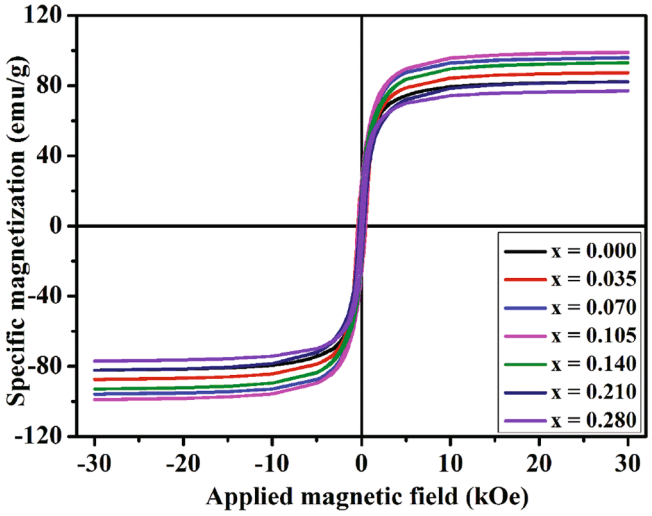

Fig. 3. Room temperature hysteresis loops of $Co_{1-x}Cd_xFe_2O_4$.

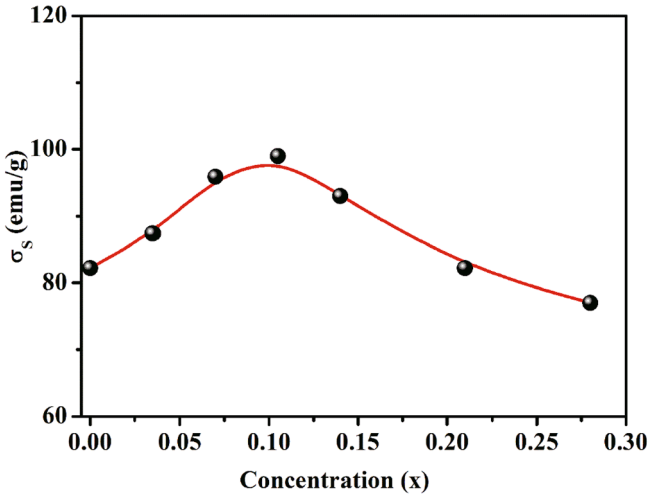

Fig. 4. Specific saturation magnetization versus cadmium concentration.

Table 2
Specific saturation magnetization (σ_S), and coercivity (H_C) of $Co_{1-x}Cd_xFe_2O_4$.

x	σ_S (emu/g)	H_C (Oe)
0.000	82.2	331
0.035	87.4	268
0.070	93.2	428
0.105	99	415
0.140	93	272
0.210	82.2	253
0.280	77	134

interaction between A and B sites. Beyond x = 0.105, Cd^{2+} ions start occupying B-sites and replace cobalt ions present at B-sites. This process dilutes the magnetic moments of both A, B-sub lattices; which is evident in a gradual decrease in Curie temperature with cadmium content. Several researchers have made the parallel observation by replacing magnetic ions with diamagnetic ones [60,61].

3.5. Cation distribution

From the above discussions, it is understood that the depletion of cobalt at A-site takes place for cadmium concentration, x = 0.105 which

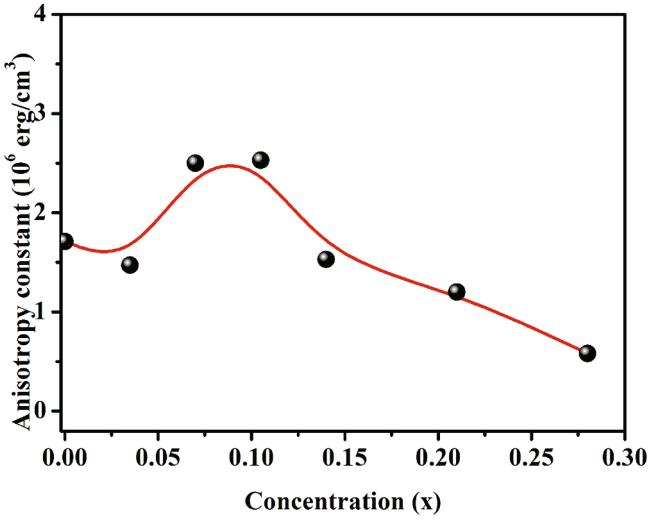

Fig. 5. Variation of anisotropy constant with cadmium content (x).

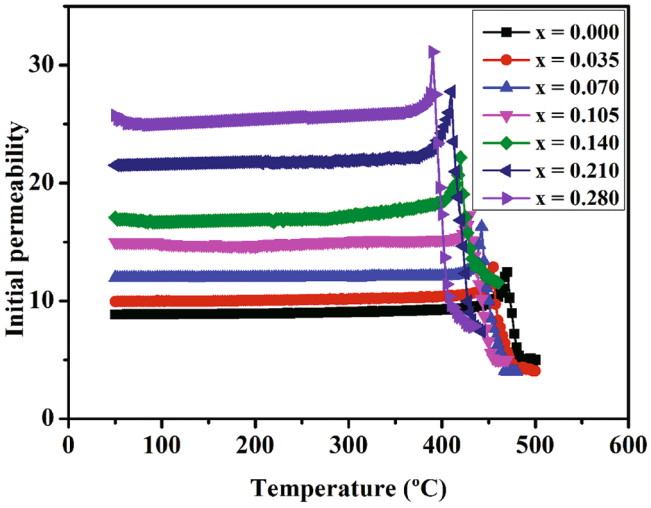

Fig. 6. Initial permeability versus temperature.

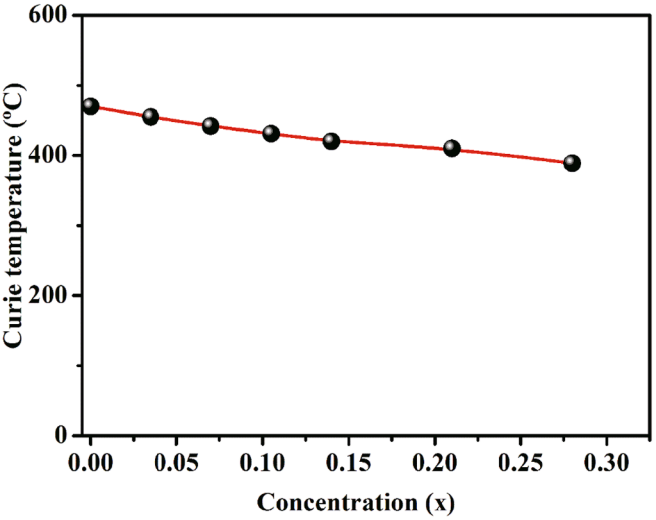

Fig. 7. Curie temperature as a function of cadmium content (x).

amounts to cobalt content 10.5% and is in agreement with that reported (11%) by Kumar et al. [62]. Considering 0.105 as the measure of inversion δ, the cation distribution for the basic composition $CoFe_2O_4$ can be written as

$$(Co_{0.105}Fe_{0.895})[Co_{0.895}Fe_{1.105}]O_4$$

The proposed distribution of the cations among tetrahedral and octahedral sites for all the samples has been mentioned in the Table 3.

The lattice constant for each composition has been computed to verify the proposed cation distribution, a correct one.

3.5.1. Lattice constant based on cation distribution

The theoretical lattice constant (a_{th}) has been calculated for each composition using the following relations [32].

$$a_{\text{Theoretical}} = \frac{8}{3\sqrt{3}}\left[(r_A + R_0) + \sqrt{3}\,(r_B + R_0)\right] \quad (4)$$

$$r_A = \text{Cobalt content} \times r_{Co^{2+}} + \text{Cadmium content} \times r_{Cd^{2+}} + \textit{Iron} \text{ content} \times r_{Fe^{3+}} \quad (5)$$

$$r_B = \frac{1}{2}\left[\textit{Cobalt content} \times r_{Co^{2+}} + \text{Cadmium content} \times r_{Cd^{2+}} + \textit{Iron} \text{ content} \times r_{Fe^{3+}}\right] \quad (6)$$

Here, $r_{Co^{2+}}$, $r_{Cd^{2+}}$ and $r_{Fe^{3+}}$ are the ionic radii (0.58 Å, 0.78 Å, 0.49 Å at A-sites and 0.745 Å, 0.95 Å, 0.645 Å at B-sites) of cobalt, cadmium and iron ions at their respective sites and oxygen ion radius (R_0) is 1.38 Å.

3.5.2. Rietveld refinement

The proposed cation distribution has been reiterated by employing Rietveld structural refinement method for all the samples of $Co_{1-x}Cd_xFe_2O_4$nanoferrite. The refinement of the diffraction patterns has been carried out using MAUD (Materials Analysis Using Diffraction) software [63]. The cations have been assigned in the A-site and B-sites as per the possibilities discussed in the magnetization section during the course of the Rietveld refinement to derive the best fit.

The refinement progress has been monitored continuously to get the minimum values of residuals such as Bragg's profile residual (R_b), weighted profile residual (R_{wp}), and expected weighted profile residual (R_{exp}). Finally, the refinement gets ended with goodness of fit (χ^2) approaching to unity [63]. The values, thus, obtained are summarized in Table 4.

The Rietveld refined XRD pattern of a typical composition $Co_{0.93}Cd_{0.07}Fe_2O_4$ has been shown in Fig. 8.

The goodness of fit (χ^2) nearly 1.5 coupled with small percentage values of residuals (R_b, R_{wp} and R_{exp}) less than 5% confirm the good agreement between theoretical and experimental data [64]. The lattice constants, obtained from the experiment, proposed cation distribution and Rietveld method for each sample of $Co_{1-x}Cd_xFe_2O_4$ are plotted in Fig. 9.

From the graph, it is clear that the lattice constants obtained from three different approaches represent the same trend with the cadmium concentration. The close agreement in lattice parameters confirms the proposed cation distributions are correct.

The accuracy of the proposed cation distribution for each sample is further confirmed by estimating the respective number of Bohr magnetons, as a function of cadmium concentration.

Table 3
Cation distribution of $Co_{1-x}Cd_xFe_2O_4$.

x	Cation distribution	
	Tetrahedral sites	Octahedral sites
0.000	$(Co_{0.105}\ Fe_{0.895})$	$[Co_{0.895}\ Fe_{1.105}]$
0.035	$(Cd_{0.035}Co_{0.070}\ Fe_{0.895})$	$[Co_{0.895}\ Fe_{1.105}]$
0.070	$(Cd_{0.070}\ Co_{0.035}Fe_{0.895})$	$[Co_{0.895}\ Fe_{1.105}]$
0.105	$(Cd_{0.105}Fe_{0.895})$	$[Co_{0.895}\ Fe_{1.105}]$
0.140	$(Cd_{0.105}Fe_{0.895})$	$[Co_{0.035}Co_{0.86}\ Fe_{1.105}]$
0.210	$(Cd_{0.105}\ Fe_{0.895})$	$[Cd_{0.105}Co_{0.790}\ Fe_{1.105}]$
0.280	$(Cd_{0.105}\ Fe_{0.895})$	$[Cd_{0.175}Co_{0.720}\ Fe_{1.105}]$

Table 4
Lattice constant, Weighted profile residual (R_{wp}), Bragg residual (R_b), expected residual (R_{exp}), and goodness of fit (χ^2).

x	Lattice constant (Å)	R_{wp}%	R_b%	R_{exp}%	χ^2
0	8.3943	2.815	2.244	1.899	1.482
0.035	8.4030	4.697	2.920	2.555	1.838
0.070	8.4138	2.017	1.591	1.300	1.552
0.105	8.4250	1.781	1.422	1.267	1.405
0.14	8.4301	1.820	1.436	1.176	1.547
0.21	8.4502	1.403	1.022	1.045	1.343
0.28	8.4729	2.174	1.509	1.274	1.707

3.5.3. Number of Bohr magnetons based on cation distribution

Based on Neel's theory of ferrimagnetism, the magnetic moment per formula unit can be calculated for each composition using the following equation from the cation distributions provided in the Table 3.

$$n_B^{cal} = M_B - M_A \quad (7)$$

M_B and M_A are the magnetic moments of B and A-sites respectively given in Bohr magnetons (μ_B). The magnetic moments of the Fe^{3+}, Co^{2+} and Cd^{2+}ions are taken as 5 μ_B, 3 μ_B and 0 μ_B respectively for calculating the magnetic moment.

The experimentally observed magnetic moment (n_B^{exp}) per formula unit in Bohr magnetons can be provided considering the specific saturation magnetization using the relation [65]

$$n_B^{exp} = \frac{M \times \sigma_S}{5585} \quad (8)$$

where M is the molecular weight in g/cm^3 and σ_S is the specific saturation magnetization in emu/g. Fig. 10 shows the variation of the experimental and the calculated magnetic moments with cadmium concentration.

Experimentally determined room temperature magnetic moment was observed to lie slightly above that calculated from the cation distributions. The magnetic moment obtained from the cation distribution refers to the magnetic moment observable at 0 K and expected to be more than that observed at room temperature because of the absence of thermal effects. The trends shown by both the magnetic moments are alike. However, to explain the detected strange behaviour, cobalt-cadmium system demands more understanding related to deviation from the stoichiometry, formation of cation–anion vacancies, and their consequent effects.

The energy dispersive X-ray analysis performed on $Co_{1-x}Cd_xFe_2O_4$ (Fig. 11) shows a slight decrease in oxygen and cadmium amounts than those expected from the stoichiometric compositions. Oxygen and cadmium were observed to have escaped very little from the samples due to the heat treatment of the samples at 1050 °C and their atomic percentages are shown in Table 5.

In the stoichiometric $Co_{1-x}\ Cd_xFe_2O_4$, the atomic percentage of oxygen should be 57.14% but the observed values lie in the range 41.38% to 54.42%. The observed reduction of cadmium, especially in the samples having concentration, x = 0.21 and x = 0.28 reveals volatilization due to its low melting point. Although incoherent amounts are seen with respect to concentration, slight loss of anion and cations has been evident from the analysis of EDX.

Based on the work done by K.A. Mohammed et al., and Zdorovets et al. [66,67] packing factors (P_a, P_b), and total vacancy concentration, β can be estimated using the cation radii and lattice parameters for each

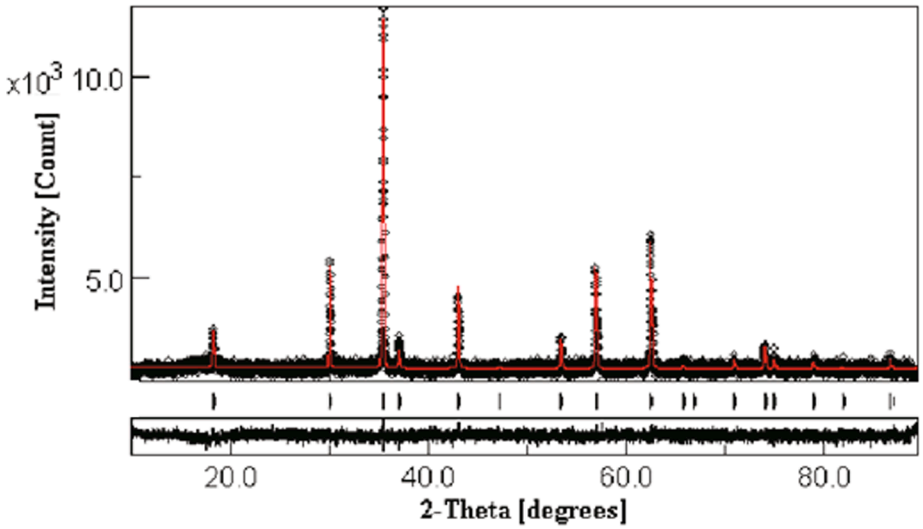

Fig. 8. Rietveld refinement of $Co_{0.93}Cd_{0.07}Fe_2O_4$.

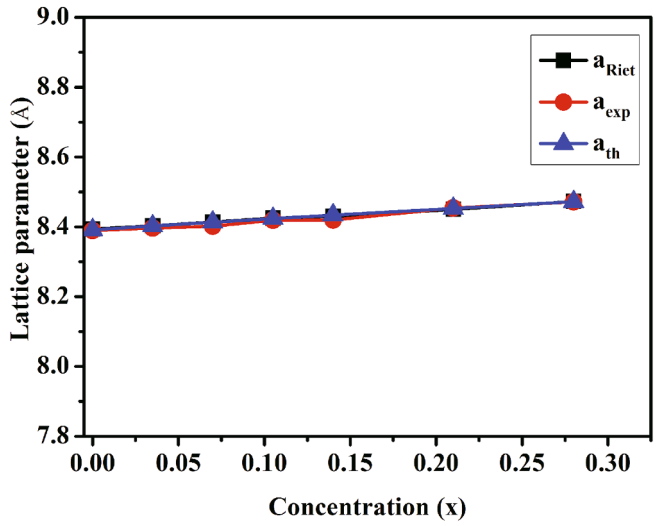

Fig. 9. Variation of the lattice parameters as a function of cadmium concentration.

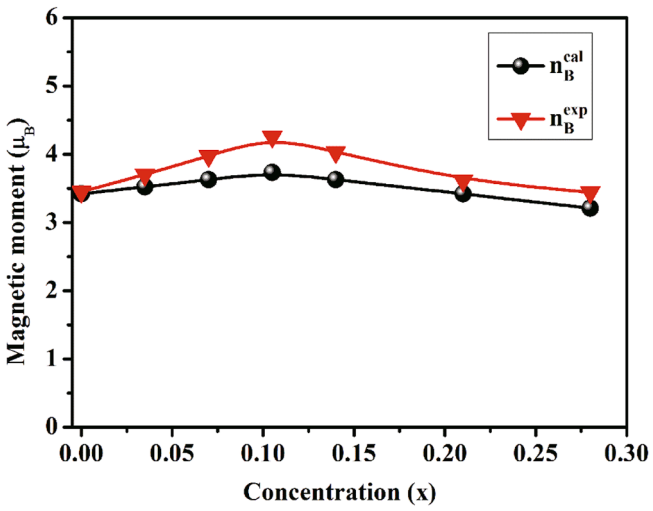

Fig. 10. Calculated and experimental magnetic moments with cadmium content (x).

composition of $Co_{1-x}Cd_xFe_2O_4$. The estimated P_a and P_b are less than 1 but close to 1 suggest the vacancies present in the samples are too less to show any detectable changes in the crystal structure. Mikhail G. Brik et al., [68] and T. Satoh & T. Tsushima [69] also reported the presence of vacancies in smaller amounts without much structural distortion. A parameter known as fulfilment coefficient of the unit cell α, estimated using octahedral, tetrahedral and oxygen ionic radii shows that with increasing cadmium concentration, Co-Cd ferrite transforms to inverse spinel structure indicating the occupancy of cadmium ions at B-sites which asserts the proposed cation distribution [68,70].

The loss of oxygen in the sample due to high preparation temperature promotes the conversion of trivalent iron into divalent one to the amount equal to its loss [71]. If the loss of oxygen and cadmium happens in equal amounts, formation of divalent iron does not exist. As the observed loss of the ions is meagre, small amount of divalent iron might be available in the sample. Perhaps, the observed increase in lattice constant might include the influence of divalent iron of larger radius than Fe^{3+} besides the effect of cadmium (section 3.1).

In complex oxides, it is said that the particle size distribution and the occurrence of the oxygen vacancies influence the exchange interaction among cations [72–74]. The observed decrease in coercivity with decreasing particle size, especially below 10 nm (Table 2) reduces the magnetic interaction between the neighbouring particles and confining the interaction to the individual particle.

The study related to the occurrence of high saturation magnetization in zinc ferrite thin films [75] and the analysis lying in understanding the excess net magnetic moment of nickel ferrite [76] highlight the oxygen vacancies created and consequent ferromagnetic interaction among the octahedral cations which forms the basis for the increase in the net magnetic moment of the sample. In the present study, the experimentally observed room temperature higher magnetic moment could be because of the ferromagnetic interaction developed between the cations existing at B-sites. The observed fall of Curie temperature with cadmium concentration (section 3.4) at a slower pace than that reported by other researchers [44,77–79] might be connected to the onset of ferromagnetic interaction due to oxygen vacancy creation.

3.6. DC resistivity

Fig. 12 shows the variation of DC resistivity measured at 100 °C as a function of cadmium concentration. Initial small increase followed by a

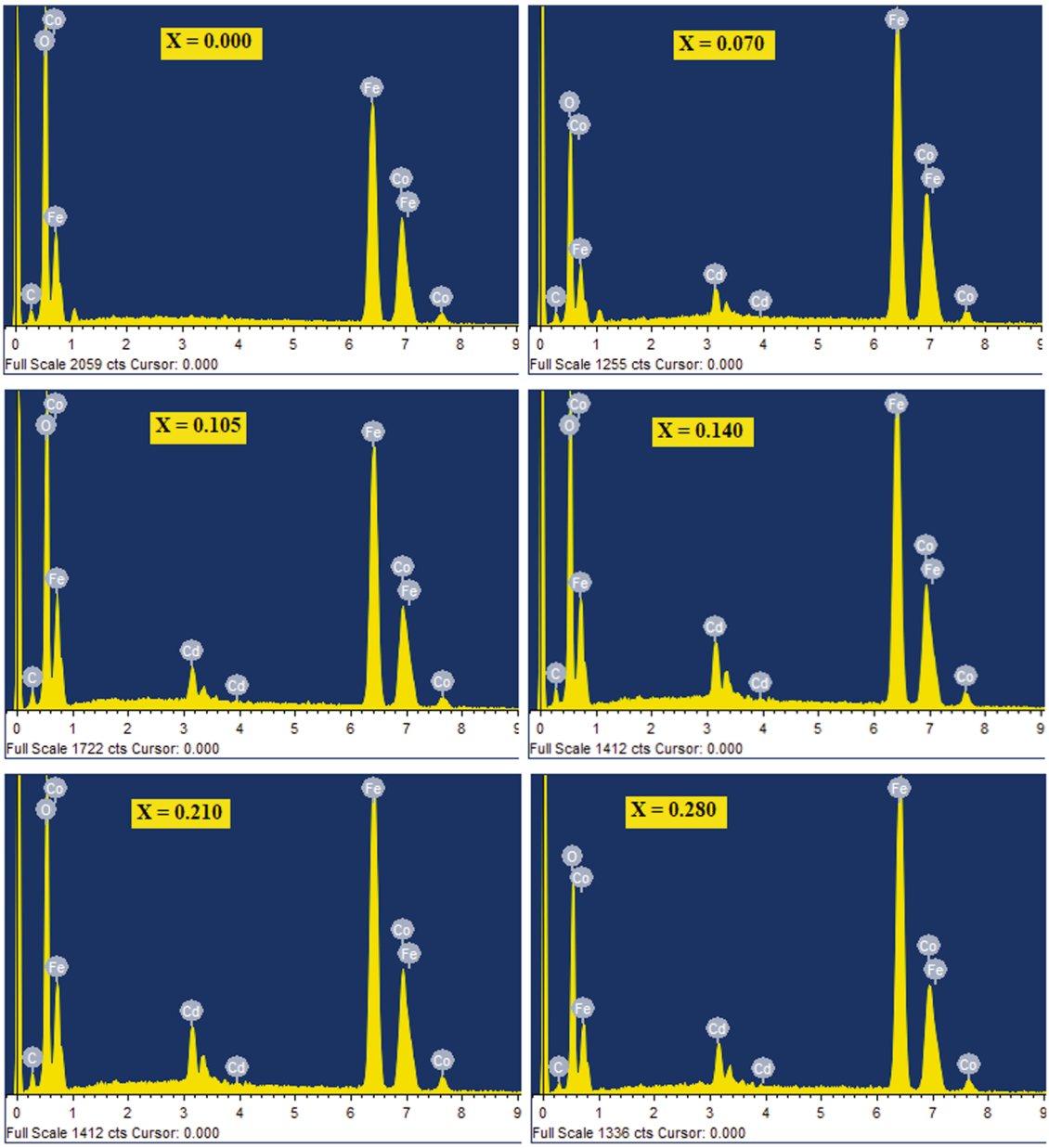

Fig. 11. EDX spectra of $Co_{1-x}Cd_xFe_2O_4$.

Table 5
Oxygen and cadmium atomic percentages of $Co_{1-x}Cd_xFe_2O$.

x in $Co_{1-x}Cd_xFe_2O_4$	Oxygen atomic percentage		Cadmium atomic percentage	
	EDX	calculated	EDX	calculated
0.000	54.02	57.14	0	0
0.070	41.38	57.14	1.21	1
0.105	54.42	57.14	1.17	1.5
0.140	52.37	57.14	1.9	2
0.210	45.66	57.14	1.76	2.5
0.280	46.33	57.14	1.82	3

sharp rise to a larger value, 1.34×10^{11} Ω-cm above the concentration x = 0.105 was observed and the rise is nearly four orders greater in magnitude than that reported 7.9×10^6 Ω-cm for Co-Cd nanoferrite measured at 50 °C [80].

The prime cause for the observed rise in resistivity may be ascribed to electron hopping between ion pairs of the same element having different valence states at B-sites [1]. As said in section 3.5.3, the formation of divalent and trivalent iron pairs might be feasible in the sample due to loss of oxygen at elevated annealing temperatures. As pointed out earlier, the substitution of cadmium impurity in place of cobalt increases the lattice constant throughout its concentration due to its higher ionic radius and thus cadmium blocks the hopping process between Fe^{2+} and Fe^{3+} ions at B-sites. The observed sharp rise in resistivity beyond x = 0.105 reiterates the accommodating nature of Cd^{2+} ions at B-sites after the complete exhaustion of cobalt ions at tetrahedral sites. As mentioned in section 3.2, the number of grains and grain boundaries formed due to the reduction in the particle size and the porosity collectively contribute to the observed phenomenal rise in resistivity of the samples [32,36,81].

The linear plots of log ρ versus 1/T for all the samples, shown in the Fig. 13 reveal the semiconducting nature of the samples. The activation energy values, determined from the slopes of these plots ranging from 0.52 eV to 0.72 eV with the varying cadmium concentration are in accordance with those reported for the nano ferrite materials [82,83].

With the attainment of required characteristics (high specific

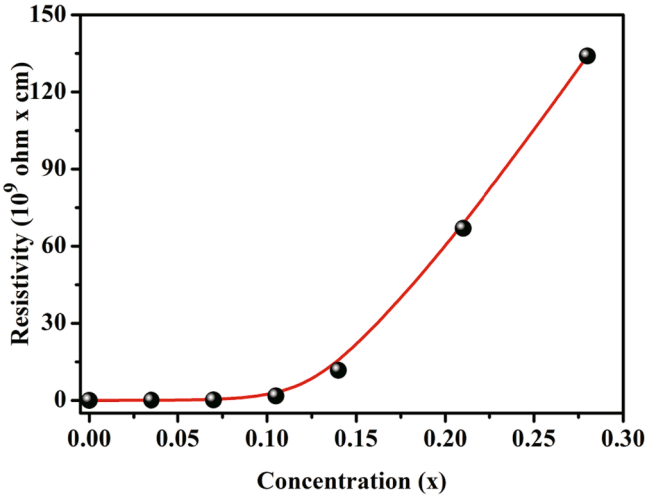

Fig. 12. DC resistivity versus concentration of the cadmium.

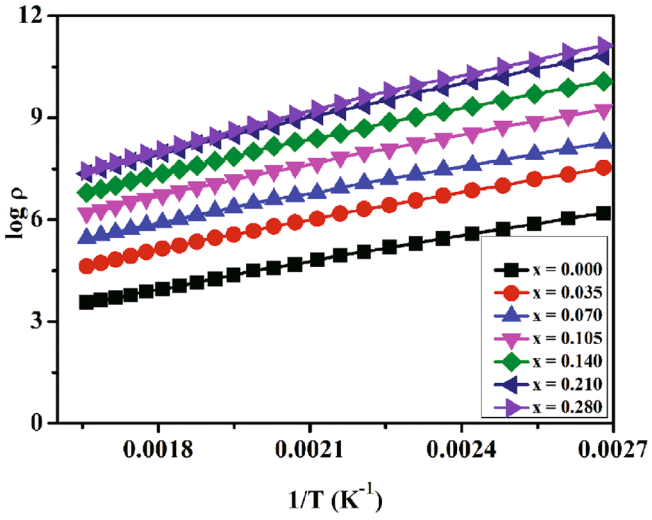

Fig. 13. log ρ versus 1/T plots.

saturation magnetization, high DC resistivity, and smaller particle size) for high frequency applications, it is envisaged that the cadmium substituted cobalt ferrite materials would capable in shifting the operational frequency to GHz for which the permeability dispersion study has been carried out in the following section.

3.7. Initial permeability

Fig. 14 shows the variation of real and imaginary parts of initial permeability with frequency for all the samples in the frequency range from 1 MHz to 3 GHz. The real and imaginary parts of initial permeability have been noticed to remain constant with the frequency variation up to 1 GHz for all the samples except the samples having concentrations x = 0.000 and x = 0.140. A small peak associated with these two samples (x = 0.000 and x = 0.140) around 1 GHz is attributed to the spin resonance that occurs naturally in ferrites due to anisotropy field [14,84]. The spin resonance peak was not observed in other cadmium substituted samples though the permeability measurements were carried up to the maximum frequency limit (3 GHz) of the instrument. The real permeability values fall in between 8 and 14 were found higher than those reported recently for nickel-zinc ferrite studied in the GHz range [14]. For the sample having cadmium concentration x = 0.280, the observed lower permeability has been attributed to high porosity.

The initial permeability dispersion is characterized by domain wall displacement and domain wall rotation [85]. The domain wall displacement is of resonant type and is significant in the low frequency range. The spin rotation that occurs in single domain particle at high frequency (GHz) is of relaxation type. The occurrence of high frequency dispersion has been thought of due to single domain particles.

Thus, the indication of the high operational frequency of the selected composition is the manifestation of the improved properties, namely, high specific saturation magnetization, high DC resistivity, least particle size and moderate permeability which together play an important role in shifting the operational frequency to GHz.

4. Conclusions

The sol–gel method demonstrated its ability to provide smaller particles coupled with improved specific saturation magnetization and DC resistivity throughout the cadmium concentration studied. Exceptional growth in DC resistivity has been observed with the incorporation of cadmium content. The study has established the occupancy of cadmium ions at tetrahedral sites is about 5.25 mol%. The accuracy of the cation distribution has been checked by finding the agreement between the experimental and calculated lattice constants. The frequency dispersion of the real part of initial permeability reveals that the operating frequency is shifted up to GHz range in all the studied samples. The improvement in the DC resistivity and specific saturation magnetization for smaller particles demonstrates the Co-Cd nanoferrites justify their application as a promising core material at high frequencies.

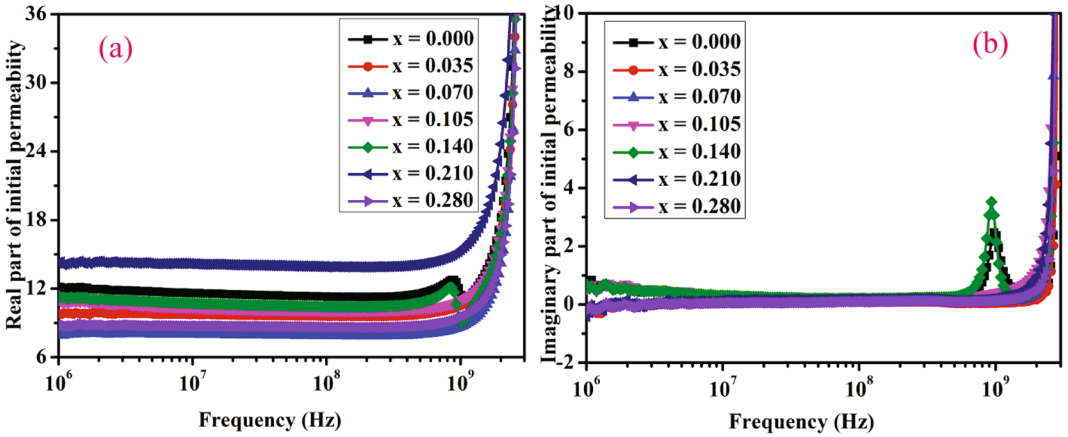

Fig. 14. Variation of (a) real and (b) imaginary permeability with frequency from 1 MHz to 3 GHz.

5. Prime novelty statement

The present work is aimed at the possibility of developing a composition suitable for high frequency operation as a magnetic core through an extensive understanding of cantion distribution of cadmium substituted cobalt ferrite. Sol-gel process has been adopted with poly-vinyl alcohol (PVA) as chelating agent to produce particles of sizes 5.7 nm and 17 nm. The samples have shown high specific saturation magnetization as well as high DC resistivity. The frequency dispersion of the real part of initial permeability reveals that the operating frequency is shifted up to GHz range in all the studied samples. The improvement in the DC resistivity and specific saturation magnetization for smaller particles demonstrates the Co-Cd nanoferrites justify their application as a promising core material at high frequencies.

Declaration of Competing Interest

The authors declare that they have no known competing financial interests or personal relationships that could have appeared to influence the work reported in this paper.

Acknowledgements

One of the authors, TRK Pydiraju, gratefully acknowledge the UGC-DAE CSR, Indore, IIT Bombay, and CCMB, Hyderabad for providing XRD, VSM, FESEM, and TEM facilities.

References

[1] S. Jagadeesh Kumar, P. Prameela, K. Srinivasa Rao, J.N. Kiran, K.H. Rao, J. Supercond. Nov. Magn. 33 (2020) 693–705.
[2] M.A. Almessiere, Y. Slimani, H. Gunguneş, V.G. Kostishyn, S.V. Trukhanov, A. V. Trukhanov, A. Baykal, Ceram. Int. 46 (2020) 11124–11131.
[3] K. Mohit, V.R. Gupta, N. Gupta, S.K. Rout, Ceram. Int. 40 (2014) 1575–1586.
[4] S.H.A. Al Lehyani, R.A. Hassan, A.A. Alharbi, T. Alomayri, H. Alamri, Int J Adv Technol 8 (2017), 1000196 (6 pages).
[5] Ulisandra Lima Ribeiro, Ricardo Silveira Nasar, Marinalva Cerqueira Nasar, José Humberto de Araújo, Ceram. Int 44 (2018) 723–727.
[6] P. Tartaj, M.P. Morales, T. González-Carreño, S. Veintemillas-Verdaguer, C. J. Serna, J. Magn. Magn. Mater. 290–291 (2005) 28–34.
[7] G. Bulai, L. Diamandescu, I. Dumitru, S. Gurlui, M. Feder, O.F. Caltun, J. Magn. Magn. Mater. 390 (2015) 123–131.
[8] R.K. Panda, D. Behera, J. Alloys Compd. 587 (2014) 481–486.
[9] G. Schmid (Ed.), Nanoparticles: From Theory to Application, Wiley-VCH, Weinheim, Germany, 2004.
[10] G. Baldi, D. Bonacchi, M.C. Franchini, D. Gentili, G. Lorenzi, A. Ricci, C. Ravagli, Langmuir 23 (2007) 4026–4028.
[11] F.S. Yardimci, M. Şenel, A. Baykal, Mater. Sci. Eng. C 32 (2012) 269–275.
[12] T. Yadavalli, H. Jain, G. Chandrasekharan, R. Chennakesavulu, AIP Advances 6 (2016), 055904.
[13] D. Chahar, S. Taneja, P. Thakur, A. Thakur, J. Alloys Compd. 843 (2020), 155681.
[14] A. Mahesh Kumar, K. Srinivasa Rao, M. Chaitanya Varma, K.H. Rao, J. Magn. Magn. Mater. 471 (2019) 262–266.
[15] R. Mondal, S. Dey, S. Majumder, A. Poddar, P. Dasgupta, S. Kumar, J. Magn. Magn. Mater. 448 (2018) 135–145.
[16] V. Kusigerski, E. Illes, J. Blanusa, S. Gyergyek, M. Boskovic, M. Perovic, V. Spasojevic, J. Magn. Magn. Mater. 475 (2019) 470–478.
[17] A. Ghasemi, E. Ghasemi, E. Paimozd, J. Magn. Magn. Mater. 323 (2011) 1541–1545.
[18] D. Lim, H. Kong, C. Lim, N. Kim, Sang Eun Shim, Sung-Hyeon Baeck, Int. J. Hydrogen Energ. 44 (2019) 23775–23783.
[19] Xian Ming Liu, Fu Shao Yun, Hong Mei Xial, Chuan Jun Huang, Physica B 370 (2005) 14–21.
[20] M.A. Almessiere, A.V. Trukhanov, Y. Slimani, K.Y. You, S.V. Trukhanov, E. L. Trukhanova, F. Esa, A. Sadaqat, K. Chaudhary, M. Zdorovets, A. Baykal, Nanomaterials 9 (2019) 202.
[21] M.V. Zdorovets, A.L. Kozlovskiy, Study of phase transformations in $Co/CoCo_2O_4$ nanowires, J. Alloys Compd 815 (2020), 152450.
[22] K. Srinivasa Rao, S.V. Ranga Nayakulu, M. Chaitanya Varma, G.S.V.R.K. Choudary, K.H. Rao, J. Magn. Magn. Mater. 451 (2018) 602–608.
[23] R. Nongjai, K. Shakeel Khan, Hilal Ahmed Asokan, Imran Khan, J. App. Phys. 112 (2012), 084321.
[24] P. AppaRao, K. SrinivasaRao, T.R.K. Pydiraju, Govinda Kapusetti, M. Mounika Choppadandi, Chaitanya Varma, K.H. Rao, J. Alloys Compd. 794 (2019) 60–67.
[25] M.A. Almessiere, A.V. Trukhanov, F.A. Khan, Y. Slimani, N. Tashkandi, V. A. Turchenko, T.I. Zubar, D.I. Tishkevich, S.V. Trukhanov, L.V. Panina, A. Baykal, Cerm. Int. 46 (2020) 7346–7354.
[26] D.I. Tishkevich, I.V. Korolkov, A.L. Kozlovskiy, M. Anisovich, D.A. Vinnik, A. E. Ermekova, A.I. Vorobjova, E.E. Shumskaya, T.I. Zubar, S.V. Trukhanov, M. V. Zdorovets, A.V. Trukhanov, J. Alloys Compd. 797 (2019) 573–581.
[27] K. Dukenbayev, I.V. Korolkov, D.I. Tishkevich, A.L. Kozlovskiy, S.V. Trukhanov, Y. G. Gorin, E.E. Shumskaya, E.Y. Kaniukov, D.A. Vinnik, M.V. Zdorovets, M. Anisovich, A.V. Trukhanov, D. Tosi, C. Molardi, Nanomaterials 9 (2019) 494.
[28] Hamid Ghayour, Majid Abdellahi, Neriman Ozada, Saeid Jabbrzare, Amirsalar Khandan, J. Phys. Chem. Solids 111 (2017) 464–472.
[29] S.V. Trukhanov, A.V. Trukhanov, V.G. Kostishyn, L.V. Panina, V.A. Turchenko, I. S. Kazakevich, V. An, E.L. Trukhanov, V.O. Natarov Trukhanova, A.M. Balagurov, J. Magn. Magn. Mater. 426 (2017) 554–562.
[30] A.L. Kozlovskiy, I.E. Kenzhina, M.V. Zdorovets, Ceram. Int. 46 (2020) 10262–10269.
[31] N. Ambikeswari, S. Manivannan, J. Alloys Compd. 763 (2018) 711–718.
[32] K. Srinivasa Rao, P. Appa Rao, M. Chaitanya Varma, K.H. Rao, J. Alloys Compd. 750 (2018) 838–847.
[33] Sheenu Jauhar, N. Ankita Goyal, Kailash Chandra Lakshmi, Sonal Singhal, Mater. Chem. Phys. 139 (2013) 836–843.
[34] Saadia Rasheed, Hafiz Sartaj Aziz, Rafaqat AliKhan, Asad Muhammad Khan, Abdur Rahim, Jan Nisar, Syed Mujtaba Shah, Farasat Iqbal, Abdur Rahman Khan, Ceram. Int. 42 (2016) 3666–3672.
[35] Rabia Ahmad, Iftikhar Hussain Gul, Muhammad Zarrar, Humaira Anwar, Muhammad Bilalkhan Niazi, Azim Khan, J. Magn. Magn. Mater. 405 (2016) 28–35.
[36] Santosh Bhukal, S. Bansal, Sonal Singhal, Physica B 445 (2014) 48–55.
[37] Santosh Bhukal, S. Tsering Namgyal, S. Bansal Mor, Sonal Singhal, J. Mol. Struct. 1012 (2012) 162–167.
[38] C. Venkataraju, G. Sathish Kumar, K. Sivakumar, J. Magn. Magn. Mater. 323 (2011) 1817–1822.
[39] Sonal Singhal, Rimi Sharma, Tsering Namgyal, Sheenu Jauhar, Santosh Bhukal, Japinder Kaur, Ceram. Int. 38 (2012) 2773–2778.
[40] P. Chandramohan, M.P. Srinivasan, S. Velmurugan, S.V. Narasimhan, J. Solid State Chem. 184 (2011) 89–96.
[41] G.S.N. Rao, B. Parvatheeswara Rao, O.F. Caltun, Mater. Today: Proceedings 2 (2015) 2491–2495.
[42] M.A. Amer, O.M. Hemeda, Hyperfine Interact. 96 (1995) 99–109.
[43] K. Srinivasa Rao, A. Mahesh Kumar, M. Chaitanya Varma, G.S.V.R.K. Choudary, K. H. Rao, J. Alloys Compd 488 (2009) L6–L9.
[44] Saroaut Noor, M.A. Hakim, S.S. Sikder, S. Manjura Hoque, Kazi Hanium Maria, Per Nordblad, J. Phys. Chem. Solids 73 (2012) 227–231.
[45] S.A. Patil, V.C. Mahajan, A.K. Ghatage, S.D. Lotke, Mater. Chem. Phys. 57 (1998) 86–91.
[46] S.R. Naik, A.V. Salker, S.M. Yusuf, S.S. Meena, J. Alloys Compd 566 (2013) 54–61.
[47] M.A. Gabal, S.S. Ata-Allah, Mater. Chem. Phys. 85 (2004) 104–112.
[48] Talat Zeeshan, Safia Anjum, Salma Waseem, Madeeha Riaz, Rehana Zia, Ceram. Int. 46 (2020) 3935–3943.
[49] Fatemeh Zamani, Amir Hossein Taghvaei, Ceram. Int. 44 (2018) 17209–17217.
[50] A.M. Abdeen, O.M. Hemeda, E.E. Assem, M.M. El-Sehly, J. Magn. Magn. Mater. 238 (2002) 75–83.
[51] Bharati R Rehani, P.B. Joshi, Kirit N. Lad, Arun Pratap, Indian J. Pure Appl. Phys. 44 (2006) 157–161.
[52] P.V. Ramana, K. Srinivasa Rao, K.H. Rao, J. Magn. Magn. Mater. 465 (2018) 747–755.
[53] Vinod Kumar, Anu Rana, M.S. Yadav, R.P. Pant, J. Magn. Magn. Mater. 320 (2008) 1729–1734.
[54] Smitha Thankachan, Binu P. Jacob, Sheena Xavier, E.M. Mohammed, J. Magn. Magn. Mater. 348 (2013) 140–145.
[55] Radheshyam Rai, Kavita Verma, Seema Sharma, Swapna S. Nair, Manuel Almeida Valente, Andrei L. Kholkin, Nikolai A. Sobolev, J. Alloys Compd. 509 (2011) 7585–7590.
[56] M. Rahimi, M. Eshraghi, P. Kameli, Ceram. Int 40 (2014) 15569–15575.
[57] Santosh Bhukal, S. Bansal SumanMor, Jagdish Singh, Sonal Singhal, J. Mol. Struct. 1071 (2014) 95–102.
[58] Syed Ismail Ahmad, Shakeel Ahmed Ansari, D. Ravi Kumar, Mater. Chem. Phys. 208 (2018) 248–257.
[59] S.S. Shinde, K.M. Jadhav, J. Mater. Sci. Lett. 17 (1998) 849–851.
[60] G. Sathish Kumar, C. Venkataraju, K. Sivakumar, J. Mater Sci: Mater Electron 24 (2013) 1057–1062.
[61] Suman Kumar Nath, Kazi Hanium Maria, S.S. Saroaut Noor, S. Manjura Sikder Hoque, M.A. Hakim, J. Magn. Magn. Mater. 324 (2012) 2116–2120.
[62] Lawrence Kumar, Pawan Kumar, Manoranjan Kar, J. Alloys Compd. 551 (2013) 72–81.
[63] Saulo Gregory Carneiro Fonseca, Laédna Souto Neiva, Maria Aparecida Ribeiro Bonifácio, Paulo Roberto Cunha, Ubiratan dos Santos, Correia Silva, João Bosco Lucena de Oliveira, Mater. Res. 21 (3) (2018), e20170861.
[64] Nejeh Hamdaoui, Yashar Azizian-Kalandaragh, Mouadh Khlifi, Lotfi Beji, J. Alloys Compd. 803 (2019) 964–970.
[65] Rajnish Kumar, Rakesh Kr. Singh, Mukesh Kumar Zope, Manoranjan Kar, Mater. Sci. Eng. B 220 (2017) 73–81.
[66] M.V. Zdorovets, A.L. Kozlovskiy, Ceram. Int. 46 (2020) 14548–14557.
[67] K.A. Mohammed, A.D. Al-Rawas, A.M. Gismelseed, A. Sellai, H.M. Widatallah, A. Yousif, M.E. Elzain, M. Shongwe, Phys. B Condens. Matter 407 (2012) 795–804.
[68] Mikhail G. Brik, Andrzej Suchocki, Agata Kamińska, Inorg. Chem. 53 (2014) 5088–5099.
[69] T. Satoh, T. Tsushima, K. Kudo, Mater. Res. Bull. 9 (1974) 1297–1300.

[70] K.A.M. Khalaf, A.D. Al-Rawas, H.M. Widatallah, K.S. Al-Rashdi, A. Sellai, A. M. Gismelseed, S.K. MohdHashim, M.S. Jameel, K.O. Al-Ruqeishi, M. Shongwe Al-Riyami, A.H. Al-Rajhi, J. Alloys Compd. 657 (2016) 733–747.
[71] S.V. Trukhanov, I.O. Troyanchuk, N.V. Pushkarev, H. Szymczak, JETP 95 (2002) 308–315.
[72] I.O. Troyanchuk, S.V. Trukhanov, D.D. Khalyavin, H. Szymczak, J. Magn. Magn. Mater. 208 (2000) 217–220.
[73] S.V. Trukhanov, A.V. Trukhanov, H. Szymczak, C.E. Botez, A. Adair, J. Low Temp. Phys. 149 (2007) 185–199.
[74] M.V. Zdorovets, I.E. Kenzhina, V. Kudryashov, A.L. Kozlovskiy, Ceram. Int. 46 (2020) 10521–10529.
[75] C.E. Rodríguez Torres, G.A. Pasquevich, P. Mendoza Zélis, F. Golmar, S.P. Heluani, Sanjeev K. Nayak, Waheed A. Adeagbo, Wolfram Hergert, Martin Hoffmann, P. Arthur Ernst, Esquinazi, S.J. Stewart, Phys. Rev. B 89 (2014) 104411.
[76] D. Elwell, R. Parker, Philos. Mag. 10 (1964) 253–261.
[77] J.J. Melo Quintero, K.L. Salcedo Rodríguez, C.E. Rodríguez Torres, L.A. Errico, J. Alloys Compd. 775 (2019) 1117–1128.
[78] C.E. Rodríguez Torres, G.A. Pasquevich, P. Mendoza Zélis, F. Golmar, S.P. Heluani, Sanjeev K. Nayak, Waheed A. Adeagbo, Wolfram Hergert, Martin Hoffmann, Arthur Ernst, P. Esquinazi, S.J. Stewart, Phys. Rev. B 89 (2014) 104411.
[79] S. Ayyappan, S. Philip Raja, C. Venkateswaran, John Philip, Baldev Raj, Appl. Phys. Lett. 96 (2010) 143106.
[80] K.S. Lohar, S.M. Patange, M.L. Mane, Sagar E. Shirsath, J. Alloys Compd. 1032 (2013) 105–110.
[81] S.V. Trukhanov, A.V. Trukhanov, A.N. Vasil'ev, A. Maignan, H. Szymczak, JETP Lett. 85 (2007) 507–512.
[82] R.K. Panda, R. Muduli, G. Jayarao, D. Sanyal, D. Behera, J. Alloys Compd. 669 (2016) 19–28.
[83] P.N. Vasambekar, C.B. Kolekar, A.S. Vaingankar, J. Mater. Sci: Mater. Electron. 10 (1999) 667–671.
[84] A. Globus, J. Phys. Colloq. 38 (C1) (1977) C1-1-C1-15.
[85] Ch. Sujatha, K. Venugopal Reddy, K. Sowri Babu, A. Rama Chandra Reddy, M. Buchi Suresh, K.H. Rao, J. Magn. Magn. Mater. 340 (2013) 38–45.